https://doi.org/10.1038/s41586-019-1073-y

Ultrafast spin-lasers

Markus Lindemann[1]*, Gaofeng Xu[2], Tobias Pusch[3], Rainer Michalzik[3], Martin R. Hofmann[1], Igor Žutić[2] & Nils C. Gerhardt[1]*

Lasers have both ubiquitous applications and roles as model systems in which non-equilibrium and cooperative phenomena can be elucidated[1]. The introduction of novel concepts in laser operation thus has potential to lead to both new applications and fundamental insights[2]. Spintronics[3], in which both the spin and the charge of the electron are used, has led to the development of spin-lasers, in which charge-carrier spin and photon spin are exploited. Here we show experimentally that the coupling between carrier spin and light polarization in common semiconductor lasers can enable room-temperature modulation frequencies above 200 gigahertz, exceeding by nearly an order of magnitude the best conventional semiconductor lasers. Surprisingly, this ultrafast operation of the resultant spin-laser relies on a short carrier spin relaxation time and a large anisotropy of the refractive index, both of which are commonly viewed as detrimental in spintronics[3] and conventional lasers[4]. Our results overcome the key speed limitations of conventional directly modulated lasers and offer a prospect for the next generation of low-energy ultrafast optical communication.

Global internet traffic will continue its remarkable increase in the near future[5]. Short-range and energy-efficient optical communication networks provide most of the communication bandwidth to secure the digital revolution. Key devices for high-speed optical interconnects—in particular, in server farms—are current-driven intensity-modulated vertical-cavity surface-emitting lasers (VCSELs)[4]. Analogous to a driven damped harmonic oscillator, modulated lasers have a resonance frequency f_R for the relaxation oscillations of the light intensity[6]. For higher frequencies the response decays and reaches half of its low-frequency value at $f_{3dB} \approx \sqrt{1+\sqrt{2}}\, f_R$, which quantifies the usable frequency range[4]. In conventional VCSELs, the modulation bandwidth is limited by the dynamics of the coupled carrier–photon system and by parasitic as well as thermal effects. The current record[7] is $f_{3dB} = 35$ GHz. Common approaches to enhance the bandwidth rely on the expression $f_R = \sqrt{v_g a S/\tau_p}/(2\pi)$, where v_g is the group velocity, a the differential gain, S the photon density and τ_p the photon lifetime[4]. S can be increased with higher pump current and smaller mode volume, τ_p can be decreased with lower mirror reflectivities and a can be optimized by material engineering. Alternative concepts to overcome the bandwidth bottleneck—the bandwidth limitations for the global internet traffic—are actively pursued, for example, in coupled-cavity VCSEL arrays[8] or photonic crystal nanocavity lasers where $f_R > 100$ GHz was attained at cryogenic temperature[9].

Unlike the above approaches that focus on the modulation of carrier and photon densities, we consider spin-lasers, which harness carrier spin and photon spin to improve their operation[10–15]. Through the conservation of total angular momentum, the spin imbalance of carriers (spin polarization) in the active region of a VCSEL is transferred to photons as circularly polarized emitted light with polarization degree[3] $P_C = (S^+ - S^-)/(S^+ + S^-)$, where $S^{+(-)}$ is the right (left) circularly polarized photon density. The relation between light polarization and spin polarization of recombining carriers is given by the dipole selection rules[3].

Although recent advances in spintronics show a versatile control of light polarization[16] and terahertz generation[17], the ultrafast operation of spin-lasers and its fundamental limitations including power consumption are largely unexplored. This provides enormous potential to investigate how using the spin could improve the operation of spin-lasers, even beyond laser diodes—to systems such as quantum cascade lasers[18] (QCLs) or external cavity lasers[19–21] that resemble an overdamped harmonic oscillator without resonant frequency (see Methods). A tantalizing prediction of spin-laser theory is that modulating the polarization of light can be realized much faster than intensity modulation (IM) and can thus overcome the limitations imposed by the f_R of coupled carrier–photon systems[22]. Here we experimentally demonstrate that adding spin-polarized carriers in conventional VCSELs supports room-temperature polarization oscillations (POs) with frequencies >200 GHz, resulting in a polarization modulation (PM) bandwidth >240 GHz, which is nearly an order of magnitude larger than that of the corresponding intensity dynamics. We show that even

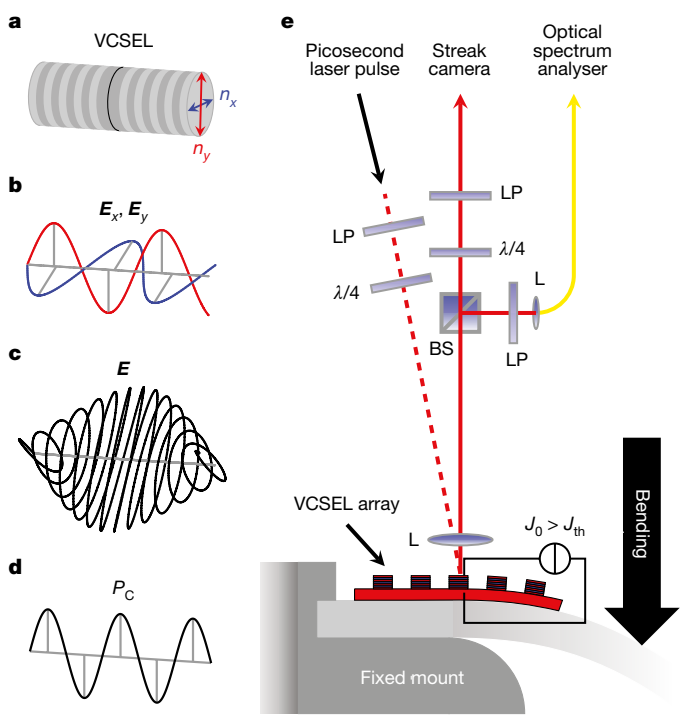

Fig. 1 | Birefringent VCSEL and measurement set-up. a, VCSEL structure with two polarization-dependent refractive indices, n_x and n_y. **b**, Linearly polarized electric field $\boldsymbol{E}_x$ and $\boldsymbol{E}_y$ with frequency difference Δf (depicted duration is much less than $1/\tilde{f}_R$). **c**, Total electric field ($\boldsymbol{E}$) oscillating between right and left circular polarization (depicted duration is $1/\tilde{f}_R$). **d**, Resulting P_C showing polarization oscillations (depicted duration is $2.5/\tilde{f}_R$). **e**, Schematic of experimental design with linear polarizer (LP), quarter-wave plate (λ/4), lens (L) and beam splitter (BS). The laser is operated with both a pumping current J_0 above threshold J_{th} and pulsed optical spin injection (dashed red line). The VCSEL emission is depicted as solid red lines and propagates towards both streak camera and fibre (yellow) coupled optical spectrum analyser. The VCSEL sample is bent as illustrated by the black arrow.

[1]Photonics and Terahertz Technology, Ruhr-Universität Bochum, Bochum, Germany. [2]Department of Physics, University at Buffalo, SUNY, Buffalo, NY, USA. [3]Institute of Functional Nanosystems, Ulm University, Ulm, Germany. *e-mail: markus.lindemann@rub.de; nils.gerhardt@rub.de

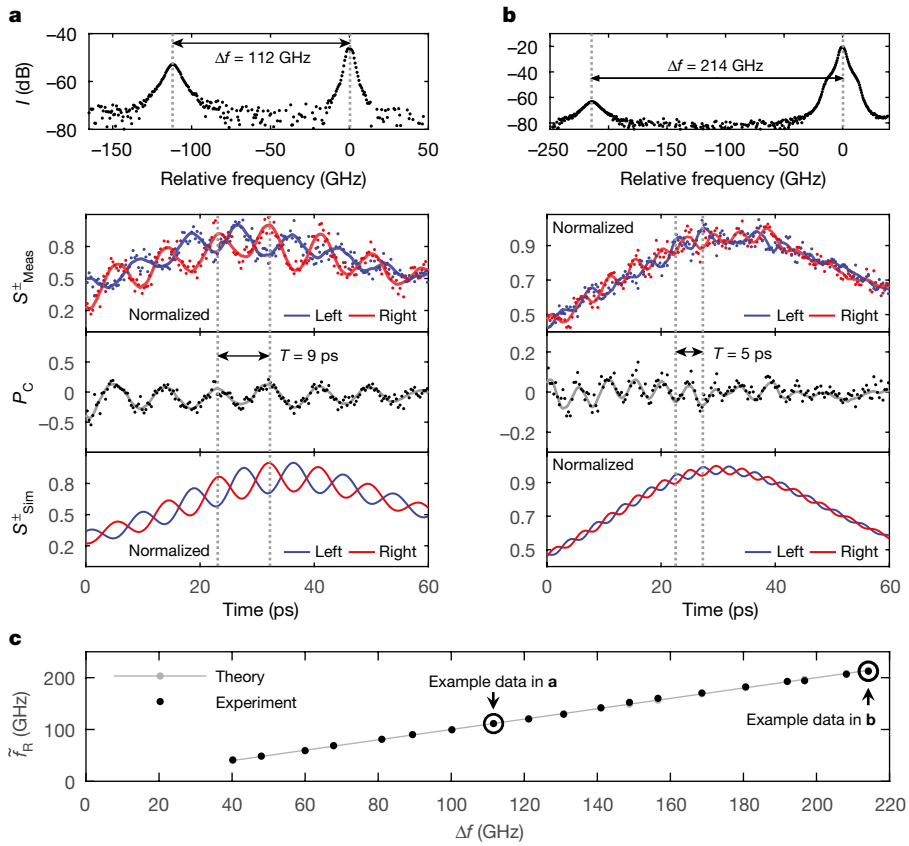

Fig. 2 | Polarization behaviour of spin-VCSELs. a, **b**, Top panel, the optical spectrum I reveals the birefringence-induced mode splitting (Δf) to be 112 GHz (**a**) and 214 GHz (**b**). The main mode (at 0 GHz) was suppressed for display. Bottom panel: $S^{\pm}_{\mathrm{Meas}}$, P_{C} and $S^{\pm}_{\mathrm{Sim}}$ are plotted against time. $S^{\pm}_{\mathrm{Meas}}$ gives the measured polarization-resolved normalized photon densities after pulsed spin injection (dots, raw data; lines, smoothed data; 'Right', $S^{+}{}_{\mathrm{Meas,Sim}}$; 'Left', $S^{-}{}_{\mathrm{Meas,Sim}}$). T denotes the period of the PO frequency. From $S^{\pm}_{\mathrm{Meas}}$, P_{C} is determined, showing the PO. $S^{\pm}_{\mathrm{Sim}}$ gives the simulated behaviour (see Methods). **c**, Plot of $\tilde{f}_{\mathrm{R}}$ against Δf, showing experimental data (dots) and results from theory (grey line). The polarization dynamics can be tuned by birefringence-induced mode splitting. Data in **a** and **b** are part of the tuning series shown in **c** (ringed dots). At $\Delta f = 214$ GHz, the frequency tuning is stopped to prevent mechanical sample damage.

for high-frequency modulation there is no need for high power. Thus an order of magnitude better energy efficiency than obtained in the best conventional VCSELs is expected. The realization of ultrafast spin-lasers provides a different path towards emerging energy-efficient room-temperature spintronic applications, not limited by magnetoresistance[3].

VCSELs show linearly polarized emission due to cavity anisotropies of refractive index $n_x \neq n_y$ (birefringence, Fig. 1a) and of absorption (dichroism). The orthogonal modes, described by electric fields $\boldsymbol{E}_x$, $\boldsymbol{E}_y$, are frequency-split by Δf due to the birefringence (Fig. 1b). Their usually weak coupling results in unstable behaviour with polarization switching and PO, which have been extensively studied and attributed to residual birefringence that is considered detrimental in both conventional and spin-lasers[4,19]. In contrast, we aim to enhance the birefringence because of its connection to the PO frequency, which is related to the beat frequency between the two orthogonal modes and leads to the periodic evolution of the total electric field $\boldsymbol{E} = \boldsymbol{E}_x + \boldsymbol{E}_y$ (Fig. 1c). P_{C} can be controlled by applying spin-polarized pumping/injection with a polarization $P_f(t) = P_0 + \delta P \sin(2\pi f t)$, where t is time, P_0 a constant offset polarization, and δP and f are the amplitude and frequency, respectively, of the modulation.

By generalizing a model for conventional VCSELs (see Methods), our theoretical analysis reveals that the PO has a resonant behaviour similar to the intensity oscillation in conventional VCSELs, but with a different frequency:

$$\tilde{f}_{\mathrm{R}} = \frac{\gamma_{\mathrm{p}}}{\pi} - \frac{\gamma S_0}{4\pi(\gamma_{\mathrm{s}}^2 + 4\gamma_{\mathrm{p}}^2)\tau_{\mathrm{p}}}(\alpha\gamma_{\mathrm{s}} - 2\gamma_{\mathrm{p}}) - \frac{\epsilon_{\mathrm{p}} S_0}{4\pi} \qquad (1)$$

where γ_{p} is the linear birefringence, γ and γ_{s} are the carrier recombination and spin-flip rates, respectively, α the linewidth enhancement factor, ϵ_{p} the phase-related saturation and S_0 the steady-state photon density normalized to its value at twice the threshold $2J_{\mathrm{th}}$. For large γ_{p}, equation (1) holds for all practical pumping regimes, while the last two terms are negligible compared with γ_{p}/π. Thus, $\tilde{f}_{\mathrm{R}} \approx \gamma_{\mathrm{p}}/\pi$ suggests that strongly enhanced birefringence may overcome the frequency limitations of conventional lasers.

Among methods to enhance birefringence—for example, using heating effects[23,24], photonic crystals or anisotropic strain[22]—we focus on mechanical bending. For this purpose we use a standard 850-nm VCSEL, which is pumped with both a direct current above J_{th} (that injects spin-unpolarized carriers) and a circularly polarized picosecond laser pulse (that excites additional spin-polarized carriers), see Fig. 1e. These pumping conditions ensure that the spin-polarized carriers are resonantly excited in the active region, to exclude influence of the split-off band[3] and to minimize heating. The time- and polarization-resolved response (f_{R} and $\tilde{f}_{\mathrm{R}}$) is detected simultaneously with a streak camera, while Δf is investigated using an optical spectrum analyser (see Methods).

Results are shown for $\Delta f = 112$ GHz ($\Delta f = 214$ GHz) in Fig. 2a (Fig. 2b). In the polarization-resolved measured and simulated normalized intensities $S^{\pm}_{\mathrm{Meas}}$ and $S^{\pm}_{\mathrm{Sim}}$, the slow envelope is the second peak of the intensity relaxation oscillation after excitation (see Methods). Its frequency is $f_{\mathrm{R}} \approx 8$ GHz for both data sets. In P_{C}, the overlaying intensity dynamics vanishes and only the fast PO is evident, showing $\tilde{f}_{\mathrm{R}} = 112\ \mathrm{GHz} \approx 14 f_{\mathrm{R}}$ or $\tilde{f}_{\mathrm{R}} = 212\ \mathrm{GHz} \approx 27 f_{\mathrm{R}}$. Remarkably, the polarization dynamics is more than an order of magnitude faster than the intensity dynamics in the same device (see Methods for relating static

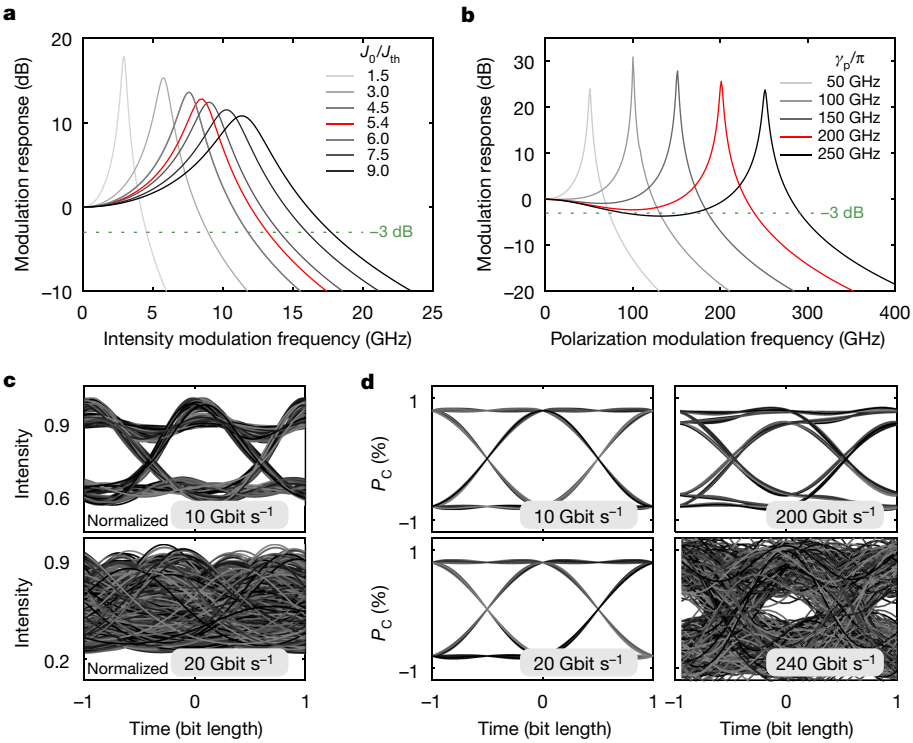

Fig. 3 | Advantage of polarization modulation in dynamic performance. **a**, Simulated intensity modulation (IM), $J(t) = J_0 + \delta J\sin(2\pi ft)$, response for varying normalized electric pumping J_0/J_{th}, where J_0 is the fixed bias current and δJ is the intensity modulation amplitude. **b**, Polarization modulation (PM), $P_J(t) = P_0 + \delta P\sin(2\pi ft)$, response for various birefringence conditions (see key). Red traces mark the simulations for the VCSEL under investigation at $\gamma_p/\pi = 200$ GHz. **c**, Eye diagrams with IM using filtered pseudorandom bit sequences for 10 Gbit s^{-1} and 20 Gbit s^{-1}. The intensity plots are normalized to their maximum values. **d**, Eye diagrams with PM for bit sequences (in Gbit s^{-1}) of 10, 20, 200 and 240 in the same device at $\gamma_p/\pi = 200$ GHz.

Δf and dynamic $\tilde{f}_R$). The PO amplitude decreases with increasing frequency, owing to both the bandwidth of the measurement system (see Methods) and fundamental limitations of the polarization dynamics including dichroism (see Methods), spin-flip rate and pumping current. By changing Δf we continuously tune $\tilde{f}_R$ up to 212 GHz, showing excellent agreement with theory over the entire frequency range (Fig. 2c). Δf and $\tilde{f}_R$ coincide within measurement accuracy (see Methods).

The demonstrated record-high PO frequency provides the basis for superior performance of spin-lasers for digital optical communication. Modulation bandwidth and data transfer rates are modelled with a parameter set carefully obtained from the PO experiments and additional measurements (see Methods). The IM response in Fig. 3a resembles the f-dependent displacement of a driven harmonic oscillator[6] with bandwidth f_{3dB}, which is enhanced (just as f_R is enhanced) by the increasing photon density produced by increased pumping. In our experiments, the pumping current of $5.4J_{th}$ corresponds to $f_{3dB} \approx 13.5$ GHz, while $f_{3dB} < 20$ GHz for all practical currents J_0/J_{th}. In contrast, Fig. 3b reveals a huge increase in PM bandwidth for the same device parameters. Similarly to $\tilde{f}_R$ in equation (1), the corresponding bandwidth $\tilde{f}_{3dB}$ increases with birefringence. Recent experiments for 1.55-μm VCSELs[25] as well as our own measurements (see Methods) confirm birefringence-tunable PM bandwidth.

To quantify the digital data transfer, a binary signal is simulated by 2^{10} pseudorandom bits. The data transfer is commonly analysed by an eye diagram[4] in which the time traces are superimposed. The central opening allows us to distinguish between '0' and '1' levels. For IM, the difference in intensities of the output light is used. Under PM, right (left) circular polarization is encoded as '1' ('0'). For the same set of VCSEL parameters and $\gamma_p/\pi = 200$ GHz, IM and PM are compared in Fig. 3c, d. The closing eye diagram precludes data transfer by IM slightly above 10 Gbit s^{-1}. PM supports data transfer up to 240 Gbit s^{-1}, showing a remarkable improvement in digital operation over conventional VCSELs, consistent with the increase of $\tilde{f}_{3dB}$ over f_{3dB}. Improvements by further increasing Δf mechanically[24,26], via photonic crystal or strained quantum-well-based VCSELs[22], potentially allow $\tilde{f}_{3dB} > 1$ THz.

Unlike common approaches in spintronics and spin-lasers[3,27] that seek to increase the spin relaxation time ($1/\gamma_s$), we find that short spin relaxation times are desirable for PM. As long as $\gamma_s \geq 2\gamma_p/\pi$, the modulation response at $f < \tilde{f}_R$ remains above −3 dB. The simulations in Fig. 4a reveal that for $\tilde{f}_R \approx 200$ GHz, γ_s is close to its optimum value. γ_s depends on the material choice[3] of the active region and the VCSEL design. For example, $\gamma_s = 1{,}000$ ns^{-1} was measured at room temperature for GaAs VCSELs (see Methods), allowing for $\tilde{f}_R > 500$ GHz. Even higher γ_s is possible in (In,Ga)As devices.

The push for faster conventional VCSELs as well as other photonic devices typically requires a stronger pumping for IM, which leads to fundamental limitations. For example, simulating the device while neglecting heating effects, an increase in pumping from $1.5J_{th}$ to $9J_{th}$ enhances f_{3dB} from 4.5 GHz to 17.8 GHz. However, higher pumping generates higher dissipated power, increasing the laser temperature. In contrast, for PM $\tilde{f}_R$ is almost independent of pumping (Fig. 4b) and only shifts from 200.1 GHz to 201.6 GHz for the same range of pumping. Thus, the highest bit rates can already be attained slightly above threshold with high energy efficiency, given by the heat-to-data ratio[28] HDR = $(P_{el} - P_{opt})$/(bit rate) with P_{el} and P_{opt} the electrical d.c. power and the optical output power, respectively. This enables ultra-low-power optical communication. In a conventional 850-nm VCSEL, a value of HDR = 56 fJ bit^{-1} at 25 Gbit s^{-1} was demonstrated[28]. Using PM for our devices, assuming pumping at $1.5J_{th}$ with electrical spin-injection, a much lower HDR = 3.8 fJ bit^{-1} could be obtained at a substantially higher bit rate of 240 Gbit s^{-1}.

Our new approach to overcome the bandwidth bottleneck in short-haul optical interconnects uses polarization to transfer information in highly birefringent spin-lasers. Even faster operation and lower values of HDR can be expected if PM is combined with high spontaneous emission coupling or threshold-less nanolasers in future optical interconnects[29]. Lasers based on two-dimensional materials[30] that support very large strain and thus high birefringence[22] may offer unprecedented bandwidths. A surprising path towards desired performance relying on a high birefringence and short spin relaxation times may also stimulate other advances and unexplored phenomena in spintronics, such as using polarization chaos in VCSELs for secure communication and high-speed random bit generators[31]. Our results show the enormous potential of spin-lasers, further motivating developing electrically pumped spin-lasers at room temperature[32]. Advances in commercial magnetic memories with a perpendicular anisotropy

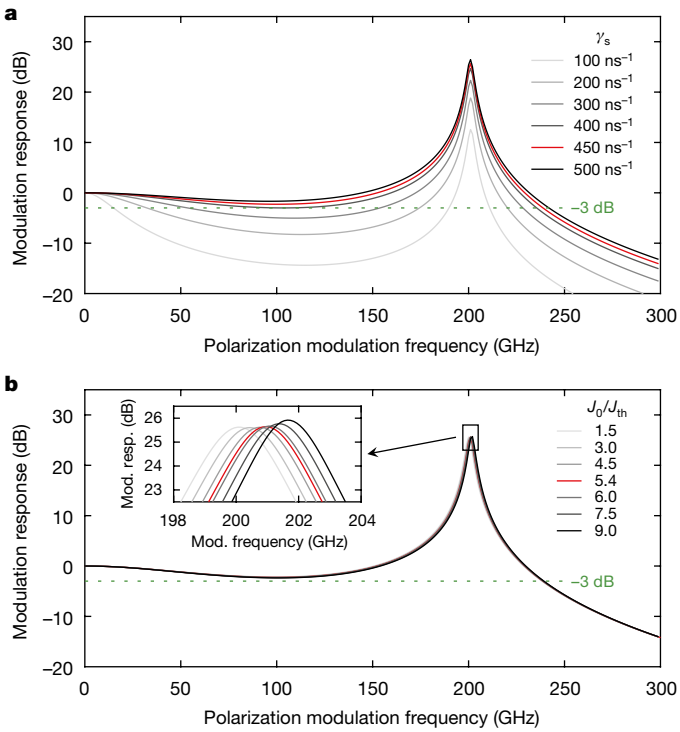

Fig. 4 | Influences on modulation bandwidth. a, Influence of spin-flip rate γ_s (see key) on modulation bandwidth, shown by plotting modulation response against polarization modulation frequency. **b**, As **a** but showing the influence of normalized electric bias J_0/J_{th} (see key). Inset, magnified view of boxed area in main plot, showing a nearly pumping-independent resonance frequency. Red traces mark the simulations for the VCSEL under investigation at $\gamma_p/\pi = 200$ GHz.

and fast magnetization switching could enable room-temperature spin injection in spin-lasers[19], provided that the underlying polarization dynamics is well understood[20]. Magnetic proximity effects in two-dimensional materials may provide an alternative path to electrically pumped spin-lasers at room temperature[33].

Online content

Any methods, additional references, Nature Research reporting summaries, source data, statements of data availability and associated accession codes are available at https://doi.org/10.1038/s41586-019-1073-y.

Received: 22 June 2018; Accepted: 28 January 2019;
Published online 3 April 2019.

1. DeGiorgio, V. & Scully, M. O. Analogy between the laser threshold region and a second-order phase transition. *Phys. Rev. A* **2**, 1170–1177 (1970).
2. Bandres, M. A. et al. Topological insulator laser: experiments. *Science* **359**, eaar4005 (2018).
3. Žutić, I., Fabian, J. & Das Sarma, S. Spintronics: fundamentals and applications. *Rev. Mod. Phys.* **76**, 323–410 (2004).
4. Michalzik, R. (ed.) *VCSELs — Fundamentals, Technology and Applications of Vertical-Cavity Surface-Emitting Lasers* (Springer, Berlin, 2013).
5. Hecht, J. The bandwidth bottleneck. *Nature* **536**, 139–142 (2016).
6. Lee, J., Oszwałdowski, R., Gøthgen, C. & Žutić, I. Mapping between quantum dot and quantum well lasers: from conventional to spin lasers. *Phys. Rev. B* **85**, 045314 (2012).
7. Haghighi, N., Larisch, G., Rosales, R., Zorn, M. & Lott, J. A. 35 GHz bandwidth with directly current modulated 980 nm oxide aperture single cavity VCSELs. In *2018 IEEE Int. Semiconductor Laser Conf. (ISLC)* https://doi.org/10.1109/ISLC.2018.8516258 (2018).
8. Fryslie, S. T. M. et al. Modulation of coherently coupled phased photonic crystal vertical cavity laser arrays. *IEEE J. Sel. Top. Quantum Electron.* **23**, 1–9 (2017).
9. Altug, H., Englund, D. & Vučković, J. Ultrafast photonic crystal nanocavity laser. *Nat. Phys.* **2**, 484–488 (2006).
10. Hallstein, S. et al. Manifestation of coherent spin precession in stimulated semiconductor emission dynamics. *Phys. Rev. B* **56**, R7076(R) (1997).
11. Holub, M., Shin, J., Saha, D. & Bhattacharya, P. Electrical spin injection and threshold reduction in a semiconductor laser. *Phys. Rev. Lett.* **98**, 146603 (2007).
12. Žutić, I. & Faria, P. E. Jr Semiconductor lasers: taken for a spin. *Nat. Nanotechnol.* **9**, 750–752 (2014).
13. Chen, J.-Y., Wong, T.-M., Chang, C.-W., Dong, C.-Y. & Chen, Y.-F. Self-polarized spin-nanolasers. *Nat. Nanotechnol.* **9**, 845–850 (2014).
14. Lindemann, M., Pusch, T., Michalzik, R., Gerhardt, N. C. & Hofmann, M. R. Frequency tuning of polarization oscillations: toward high-speed spin-lasers. *Appl. Phys. Lett.* **108**, 042404 (2016).
15. Torre, M. S. et al. High frequency continuous birefringence-induced oscillations in spin-polarized vertical-cavity surface-emitting lasers. *Opt. Lett.* **42**, 1628–1631 (2017).
16. Nishizawa, N., Nishibayashi, K. & Munekata, H. Pure circular polarization electroluminescence at room temperature with spin-polarized light-emitting diodes. *Proc. Natl Acad. Sci. USA* **114**, 1783–1788 (2017).
17. Seifert, T. et al. Efficient metallic spintronic emitters of ultrabroadband terahertz radiation. *Nat. Photon.* **10**, 483–488 (2016).
18. Faist, J. *Quantum Cascade Lasers* (Oxford Univ. Press, Oxford, 2013).
19. Frougier, J. et al. Accurate measurement of the residual birefringence in VECSEL: towards understanding of the polarization behavior under spin-polarized pumping. *Opt. Express* **23**, 9573–9588 (2015).
20. Alouini, M. et al. VSPIN: a new model relying on the vectorial description of the laser field for predicting the polarization dynamics of spin-injected V(e)CSELs. *Opt. Express* **26**, 6739–6757 (2018).
21. Baili, G. et al. Experimental demonstration of a tunable dual-frequency semiconductor laser free of relaxation oscillations. *Opt. Lett.* **34**, 3421–3423 (2009).
22. Faria, P. E. Jr et al. Toward high-frequency operation of spin lasers. *Phys. Rev. B* **92**, 075311 (2015).
23. Jansen van Doorn, A., van Exter, M. & Woerdman, J. Tailoring the birefringence in a vertical cavity semiconductor laser. *Appl. Phys. Lett.* **69**, 3635–3637 (1996).
24. Pusch, T. et al. Monolithic vertical-cavity surface-emitting laser with thermally tunable birefringence. *Appl. Phys. Lett.* **110**, 151106 (2017).
25. Yokota, N., Nisaka, K., Yasaka, H. & Ikeda, K. High-speed modulation of 1.55-μm VCSELs with spin polarization modulation. In *Conf. Lasers and Electro-Optics* https://doi.org/10.1364/CLEO_SI.2018.STu3Q.2 (Optical Society of America, 2018).
26. Pusch, T., Lindemann, M., Gerhardt, N. C., Hofmann, M. R. & Michalzik, R. Vertical-cavity surface-emitting lasers with birefringence above 250 GHz. *Electron. Lett.* **51**, 1600–1602 (2015).
27. Iba, S., Koh, S., Ikeda, K. & Kawaguchi, H. Room temperature circularly polarized lasing in an optically spin injected vertical-cavity surface-emitting laser with (110) GaAs quantum wells. *Appl. Phys. Lett.* **98**, 081113 (2011).
28. Moser, P. et al. 56 fJ dissipated energy per bit of oxide-confined 850 nm VCSELs operating at 25 Gbit/s. *Electron. Lett.* **48**, 1292–1294 (2012).
29. Jagsch, S. T. et al. A quantum optical study of thresholdless lasing features in high-β nitride nanobeam cavities. *Nat. Commun.* **9**, 564 (2018).
30. Wu, S. et al. Monolayer semiconductor nanocavity lasers with ultralow thresholds. *Nature* **520**, 69–72 (2015).
31. Raddo, T. R., Panajotov, K., Borges, B.-H. V. & Virte, M. Strain induced polarization chaos in a solitary VCSEL. *Sci. Rep.* **7**, 14032 (2017).
32. Bhattacharya, A. et al. Room-temperature spin polariton diode laser. *Phys. Rev. Lett.* **119**, 067701 (2017).
33. Žutić, I., Matos-Abiague, A., Scharf, B., Dery, H. & Belashchenko, K. Proximitized materials. *Mater. Today* **22**, 85–107 (2019).

Acknowledgements For supporting this work the authors thank the German Research Foundation (grant nos GE1231/2-2 and MI607/9-2), the US National Science Foundation (grant nos ECCS-1508873 and ECCS-1810266) and the US Office of Naval Research (grant no. 000141712793).

Reviewer information *Nature* thanks Daniel Dolfi, Hiro Munekata and the other anonymous reviewer(s) for their contribution to the peer review of this work.

Author contributions N.C.G. and M.R.H. conceived the project idea. M.L. planned and conducted the experiments and experimental analysis, and characterized the measurement system. T.P. developed the advanced laser mount and performed the device processing. R.M. devised methods of birefringence tuning of VCSELs and was involved in the device optimization. G.X. and I.Ž. developed the generalized model for simulation. M.L., G.X. and N.C.G. performed the numerical simulations. M.L., G.X., I.Ž. and N.C.G. wrote the manuscript. All authors discussed the results and revised the manuscript.

Competing interests The authors declare no competing interests.

Additional information
Extended data is available for this paper at https://doi.org/10.1038/s41586-019-1073-y.
Reprints and permissions information is available at http://www.nature.com/reprints.
Correspondence and requests for materials should be addressed to M.L. or N.C.G.
Publisher's note: Springer Nature remains neutral with regard to jurisdictional claims in published maps and institutional affiliations.

METHODS

Carrier-photon versus spin-photon dynamics for laser modulation. Current-modulated vertical-cavity surface-emitting lasers (VCSELs) are key devices for high-speed optical interconnects in today's server farms. In such conventional lasers, the modulation bandwidth is limited by the dynamics of the coupled carrier–photon system and additional parasitic and transport effects. The small-signal modulation bandwidth f_{3dB} of conventional VCSELs reached a record value of 35 GHz in 2018[7]. However, the next-generation optical emitters require a much higher modulation bandwidth to solve the bandwidth bottleneck in short-haul optical interconnects. Several concepts for fast lasers are currently under investigation to face this challenge.

Highly interesting light sources for high-speed communication are mode-locked semiconductor laser diodes[34,35]. Data rates of 100 Gbit s^{-1} have been demonstrated already[35], but these systems are much more complex and less integrated than directly modulated devices for short-haul fibre communications. Quantum cascade lasers (QCLs) may potentially allow direct modulation up to hundreds of gigahertz, enabled by the extremely short upper state carrier lifetime[18]. QCLs can have overdamped intensity dynamics (class A lasers) and thus do not show relaxation oscillation resonances in the modulation response[36]. However, an extension above the limits of conventional lasers and into the range above 100 GHz still has to be performed.

All conventional approaches mentioned so far focus on the modulation of carrier and photon densities, while the spin property of electrons and photons has not been used.

Using the coupling between carrier spin and photon spin for the development of high-speed lasers has become a field of very active research within the past years[12–15,22,37–42]. Hallstein et al.[10] revealed an impressive potential of the carrier-spin–photon dynamics in VCSELs in 1997 for the first time. They demonstrated the transfer of a coherent Larmor precession of the electron spin to the spin of the optical field and thus to the polarization of the laser emission[10]. Oscillation frequencies of 44 GHz have been presented in an external magnetic field of 4 T at cryogenic temperature. Even though this concept does not allow an arbitrary modulation of the polarization, it demonstrated the potential of the carrier-spin–photon dynamics for ultrafast devices. Together with the other advantages of spin-VCSELs such as threshold reduction[11,22,43–51], enhanced emission intensities[11,52] and polarization control[11,19,20,27,49,53–61], it stimulated the enormous research effort in this field in recent years. Within the field of modulation dynamics several studies were able to demonstrate polarization switching (PS)[37,62], an enhancement of modulation dynamics[6,63–65], improved eye diagrams and reduced chirp in spin-lasers[66]. However, so far both the achieved speed of the dynamics and the bandwidths have not been superior to those of the best conventional devices.

A key enabler to increase the polarization dynamics is to make use of cavity anisotropies in spin-VCSELs[14,22,37–39] as described in detail in this work. For over 20 years it has been known that the cavity anisotropies have an important impact on the polarization dynamics of conventional VCSELs[67–73]. The coupling between carrier-spin dynamics and cavity anisotropies in dichroism and birefringence is responsible for the rich and complex polarization dynamics of VCSELs, ranging from polarization switching to chaos[31,70,74]. Polarization oscillations at 2.1 GHz due to a mode splitting induced by residual birefringence have been discussed for 850-nm VCSELs[70,71]. Since PS basically causes excess noise and an increasing bit error rate, it is typically not desired for many applications[4]. Much research has been done on the suppression of PS and the stabilization the polarization state—for example, by including birefringence and dichroism[4,75–78]. Alternatively, PS instabilities have been discussed as an additional functionality: for example, in bistable laser diodes to achieve high repetition rates[79].

Birefringence-induced polarization oscillations of about 10 GHz after pulsed optical spin injection have been observed in VCSELs close to the polarization switching point[37,38]. These experiments demonstrated that the polarization oscillation frequency $\tilde{f}_R$ can indeed be higher than the resonance frequency f_R for the relaxation oscillations of the light intensity. However, since only the intrinsic birefringence was implemented, the frequency was limited to values considerably lower than the intensity oscillations in the best conventional lasers. It should be noted that this approach is conceptually different to that of dual-frequency lasers[21,80–82] (used, for example, as carrier frequency generators for microwave photonics applications), as well as to polarization self-switching concepts in VCSELs[83], owing to the fundamental role of spin injection and the strong carrier–spin coupling in the spin-lasers.

Based on the damped polarization oscillations in spin-VCSELs mentioned above, controlled 'on' and 'off' switching has been obtained at about 10 GHz, indicating a path for potential polarization modulation[40]. Birefringence-induced continuous oscillations of up to 11 GHz were reported in 2017 in the bistability region of an optically pumped 1.3-μm VCSEL, attributed to a Hopf bifurcation[15]. Recently, we were able to demonstrate polarization oscillations up to 44 GHz in spin-lasers[14] by inducing external strain. Since this was already comparable to the intensity dynamics of the best conventional devices, these first results stimulated interest in the potential of spin-lasers for ultrafast modulation[14,15]. However, the full potential and the fundamental limitations of spin-lasers were not revealed.

In order to demonstrate that birefringent spin-VCSELs are suitable for ultrafast polarization modulation and data transmission, four major challenges had to be overcome: (1) implementing sufficient strain-induced birefringence splitting in VCSELs; (2) proving that birefringence can control the polarization oscillation frequency; (3) demonstrating that polarization dynamics in spin-lasers can be as fast as hundreds of gigahertz, faster than other state-of-the-art concepts for direct laser modulation; and (4) verifying its capability for optical data communication. Additionally, for practical implementation it is also important to establish a low power consumption.

A high birefringence splitting can be obtained via, for example, the elasto-optic effect. Panajotov et al.[75] demonstrated values up to 80 GHz in 2000. Recently we were able to demonstrate a record value of 259 GHz for the birefringence-induced mode splitting using a direct bending approach comparable to the technique used here[26]. Even higher values have been discussed theoretically[22,84]. In order to enable fully integrated structures and electric tunability with large birefringence, an on-chip implementation based on asymmetric heating has been presented recently. Using this approach, mode splitting of more than 60 GHz with a tuning range of 45 GHz has been achieved[24]. In conclusion, sufficient birefringence can be included to potentially reach the highest frequencies. Although this is a very promising first step on the way to ultrafast spin-lasers, the investigated frequency splitting between the two orthogonal linearly polarized laser modes is only a static response, and provides no information about the dynamic behaviour of the light polarization or the spin-carrier dynamics of the system. The fundamental question of whether the spin and polarization dynamics can follow the mode splitting was still unanswered.

Our recent result (enhancing the polarization dynamics to resonance frequencies of $\tilde{f}_R = 44$ GHz by external strain[14]) was a first encouraging step, demonstrating dynamics comparable to the intensity relaxation oscillation frequency of the best conventional lasers. The work presented in the main text, in contrast to that, now demonstrates a technologically significant breakthrough of a fivefold higher oscillation frequency than previously reported in any spin-laser and even more than fivefold higher than in the best conventional lasers.

However, the use of spin-VCSELs for optical communication requires a further major innovation step, as demonstrated here. Even when a resonance frequency oscillation larger than 200 GHz is attained, there is no guarantee that it can be directly translated to a large bandwidth useful for optical communication. In contrast to the common expectation from both spin-lasers and spintronics, we show that a short spin-relaxation time is needed to realize record-high modulation bandwidth. As shown in Fig. 4 in the main text, the most intuitive strategy of simply increasing the spin-relaxation time for a better performance would not be successful but provide only a modest modulation bandwidth. However, standard III–V active materials such as GaAs are well suited to provide fast spin dynamics. In GaAs VCSELs, a spin-flip rate as high as $\gamma_s = 1{,}000$ ns^{-1} was measured at room temperature[73]. This corresponds to a spin-relaxation time of 1 ps, basically allowing modulation frequencies >500 GHz.

Correspondence of $\tilde{f}_R$, Δf and γ_p. The polarization oscillation frequency $\tilde{f}_R$, the birefringence-induced mode splitting Δf and the linear birefringence parameter γ_p are closely connected.

Δf represents the frequency difference between the two orthogonal linearly polarized modes $\boldsymbol{E}_x$ and $\boldsymbol{E}_y$. It is tuned by inducing anisotropic strain and measured via the optical spectrum. Following the generalized spin-flip model (described in detail later), Δf can be approximately described by the frequency difference between the individual, stationary x- and y-polarized modes:

$$\Delta f \approx \frac{\gamma_p}{\pi} - \frac{\alpha}{\pi}\gamma_a \tag{2}$$

Here, additional effects due to the simultaneous emission of lasing and non-lasing modes are neglected. According to equation (2), Δf principally corresponds to the effective birefringence, that is, the linear birefringence γ_p and the nonlinear birefringence represented by the linewidth enhancement factor α and the dichroism γ_a. The contributions of the phase and amplitude saturation for the individual modes are identical and thus do not influence the difference frequency. Via Δf and the parameters γ_a and α, the linear birefringence is extracted and used for the simulations with the generalized spin-flip model.

Following the picture of a spin-laser as a driven damped harmonic oscillator, the polarization oscillation frequency $\tilde{f}_R$ corresponds to the resonance frequency of the coupled spin–photon system. During the experiments, $\tilde{f}_R$ is measured by Fourier transforming the temporal traces of the circular polarization degree P_C. A theoretical analysis based on the generalized spin-flip model reveals that in resonance, the polarization basically oscillates with the beat frequency of the two orthogonal linearly polarized electric fields $\boldsymbol{E}_x$ and $\boldsymbol{E}_y$. Thus, $\tilde{f}_R$ is expected to follow

Δf as long as the coupled spin-polarization dynamics is sufficiently fast and, in particular, the spin-flip rate is sufficiently high. The experimental and theoretical verification is depicted in Fig. 2c in the main text. According to equation (1) in the main text, the resonance frequency in the perturbative regime $J \ll \gamma_p \gamma_s \tau_p / \gamma$, considering the simultaneous emission of both laser modes, can be described as:

$$\tilde{f}_R = \frac{\gamma_p}{\pi} - \frac{\gamma S_0}{4\pi(\gamma_s^2 + 4\gamma_p^2)\tau_p}(\alpha\gamma_s - 2\gamma_p) - \frac{\epsilon_p S_0}{4\pi} \quad (3)$$

For a parameter regime in which the anisotropies are dominated by the linear birefringence γ_p, an approximation for $\tilde{f}_R$ and Δf can be given from equation (2) and equation (3) as:

$$\Delta f \approx \tilde{f}_R \approx \frac{\gamma_p}{\pi} \quad (4)$$

Though Δf and $\tilde{f}_R$ are closely related, they refer to a static (Δf) and a dynamic ($\tilde{f}_R$) regime. Thus, there is a crucial difference between the static response of about 250 GHz birefringence, visible as mode splitting in the spectrum of the laser emission, reported in ref. [26], and the possibility of achieving high-frequency operation of a laser as demonstrated in the main text. As shown in this work, the crucial parameters that are potentially limiting the spin and polarization dynamics at high frequency are in particular the effective dichroism and the spin-flip rate.

The resonance frequency of the coupled carrier-spin–photon dynamics in the spin-laser $\tilde{f}_R$ can be directly investigated after pulsed spin injection. Without spin injection, in most cases only one of the linearly polarized modes is lasing while the other is strongly suppressed. Spin-polarized pumping leads to a gain anisotropy for the transitions involving spin-up and spin-down electrons, which results in a laser emission with non-zero degree of circular polarization[22,38]. In terms of the linear orthogonally polarized modes, both modes need to contribute to the circularly polarized emission. Owing to the birefringence-induced mode splitting, their frequencies are different and the resulting beating leads to polarization oscillations determined by Δf.

However, in contrast to other approaches (such as, for example, dual-frequency lasers[21,80–82]), in spin-lasers the spin dynamics in the gain material is crucial, while the carrier-intensity dynamics is mainly decoupled. The polarization oscillation feeds back to the carrier-spin system in the gain material, which results in oscillations of the whole carrier-spin–photon system. This provides a direct link to control and modulate the polarization by carrier spin injection.

While other concepts based on PS[15,83] often concentrate on the regime of bistability close to a PS point, a regime of weak coupling, polarization modulation in spin-lasers is not restricted to this but makes use of the strong coupling with large birefringence and potentially large dichroism. This establishes the capacity of spin-lasers for ultralow power consumption (see Fig. 4 in the main text).

As demonstrated in Fig. 3 of the main text, the modulation bandwidth of spin-lasers benefits from an extremely high $\tilde{f}_R$, which is tunable via the mode splitting as long as the spin dynamics are sufficiently fast. However, for a broad modulation bandwidth and high quality eye diagrams, not only the frequency is important, but also the damping of the dynamics influenced by the linear and nonlinear dichroism as described below.

The spin-VCSEL. For the experiments, a conventional AlGaAs-based 850-nm VCSEL with standard non-magnetic metal contacts for electrical spin-unpolarized pumping was used. The structure was grown on n-doped (100)-oriented GaAs substrate by Philips Photonics. It consists of three GaAs quantum wells with an approximately 4-μm oxide aperture for current confinement in the p-region close to the quantum wells. The VCSEL was operated at room temperature. It showed transverse single-mode operation at least up to 2.1 mA. Further details on the VCSEL and the mount can be found elsewhere[26,85].

As an extension of purely optical pumping approaches to spin pumping (see, for example, refs [10,42]), we employed hybrid pumping in order to investigate the intensity and polarization dynamics after pulsed spin-injection. Right circularly polarized laser pulses at 850 nm were used to excite spin-polarized carriers resonantly into the active region. The laser pulses were generated by a Ti:sapphire laser (75.6 MHz, 200 fs) and propagated through a single-mode fibre for beam shaping, leading to a pulse broadening, resulting in a pulse width of approximately 2 ps. The pulses were injected into the VCSEL with a small incidence angle (below 0.5°) to the surface normal in order to separate pump and VCSEL emission. The average power density of the pumping beam is around 500 W cm^{-2} at a spot size of approximately 40 μm. Additionally, the VCSEL was pumped electrically with a direct current of 2.1 mA. The threshold current depends on the mechanical strain applied, and varied between 0.43 mA and 0.39 mA for low and high mechanical strain. The current used corresponds to operation at 4.9 to 5.4 times the threshold current, J_{th}. The polarization is determined by a combination of linear polarizer and quarter-wave plate.

Birefringence tuning. Recently we demonstrated that the polarization dynamics of the laser can be enhanced by incorporating birefringence[14], which was induced into the VCSEL cavity via the elasto-optic effect using mechanical stress. In an optimized method, a VCSEL array of 1 mm × 1 mm containing 16 single VCSEL devices was glued onto a metal stripe using conductive glue. While one side of the metal stripe was fixed, the other could be bent, resulting in a controlled and reversible mechanical stress along the [011] crystal direction. The use of an array ensures that some of the VCSELs are located at an optimum position on the bending radius to experience maximum strain. With this approach, birefringence-induced mode splittings from 0 GHz to 226 GHz have been realized, limited by the mechanical damage threshold for the VCSEL array. The maximum value of 214 GHz presented in this Letter was chosen in order to safely avoid damage to the sample. Further details about the bending technique can be found elsewhere[85]. To give more quantitative insights into the range of strain obtained by bending, the material behaviour when subject to deflection was simulated using finite-element methods and Euler–Bernoulli beam theory.

Extended Data Fig. 1a depicts the relation between the strain $\Delta l/l$, represented by relative change in the spatial dimension and the resulting mode splitting. The maximum strain obtained is estimated to be around $\Delta l_{max}/l = 0.0034$, resulting in the linear birefringence controlled mode splitting of $\Delta f = 214$ GHz.

Unstrained sample. For comparison, we show experimental data without applied external strain. An intrinsic mode splitting of 8.4 GHz can be observed in Extended Data Fig. 1b. This mode splitting is caused both by the internal electric fields (which result in a change of the refractive index via the electro-optic effect) and by a residual internal strain or an induced strain (caused, for example, by the electrical contact or the mount) affecting the birefringence via the elasto-optic effect[69]. Such an intrinsic mode splitting is typically observed in VCSELs. As expected, a polarization oscillation can be observed with an $\tilde{f}_R$ according to the intrinsic birefringence-induced mode splitting (Extended Data Fig. 1c).

Laser dynamics and birefringence-induced mode splitting. The VCSEL emission propagates through a Stokes polarimeter set-up consisting of a rotating quarter-wave plate and a Glan–Thompson linear polarizer[86]. For simplification, two measurements were performed during which the polarizer's and the wave plate's main axes enclose angles of 45° and 135°. A streak camera (Hamamatsu C5680, S-1 cathode) samples the resulting photon density traces $S^{\pm}_{Meas}$ for opposed circular polarizations, which are normalized to maximum intensity, in order to calculate the circular polarization degree. In front of the streak camera the beam is transmitted through a grating spectrometer. The entire system offers a temporal resolution down to 2.7 ps. The sum of $S^{\pm}_{Meas}$ contains information about the intensity behaviour, whereas $P_C = (S^{+}{}_{Meas} - S^{-}{}_{Meas})/(S^{+}{}_{Meas} + S^{-}{}_{Meas})$ is mainly decoupled from the intensity dynamics. The standard deviation of the smoothed (raw) data of P_C is 1.5% (4.0%), which confirms a sufficient measurement accuracy to resolve the signal. Simultaneously, the VCSEL emission is coupled into an optical spectrum analyser (OSA) with a resolution better than 5 GHz and a relative accuracy better than ±1 GHz, in order to determine the birefringence-induced mode splitting. The timescale of the streak camera and the frequency scale of the OSA are mutually calibrated using a pulse train generated by a 200-fs Ti:sapphire laser pulse propagated through an etalon with a free spectral range of 50 GHz.

Temporal resolution. We experimentally determined the temporal resolution of our measurement system. The set-up used for this purpose comprises a Michelson interferometer in which the 200-fs Ti:sapphire laser pulses are transmitted to the entrance slit of the grating spectrometer in front of the streak camera. By means of a movable delay stage in one arm of the interferometer, a double pulse train with variable pulse delay Δt can be generated. In between the two pulses there is an intensity minimum. The intensity contrast—that is, the difference between (normalized) maximum and minimum intensities—is determined for pulse delays approaching zero. For a particular delay, the corresponding frequency Δt^{-1} is calculated. The frequency resolution depends on the grating order. Frequencies Δt^{-1} up to at least 290 GHz (180 GHz) can be resolved using the zeroth (first) diffraction order. For the measurements showing polarization dynamics above 200 GHz, the zeroth diffraction order is used in order to profit from the higher measurement bandwidth. For polarization oscillations below 200 GHz we use the first diffraction order for sensitivity reasons.

Acquisition timing. In ultrafast measurements, caused by the functional principle of the streak camera, the time window of acquisition gets much shorter than the decay time of both intensity and polarization effects. Therefore a decision must be made on the time offset at which the ultrafast polarization oscillations are acquired in relation to the excitation pulse. The chosen value has to account for the fact that during the initial pulse, Ti:sapphire laser excitation and VCSEL output are overlain, and also for the fact that the intensity in the first relaxation minimum is quite low. Best data acquisition is therefore possible during the second maximum of the intensity relaxation oscillation. This is illustrated in Extended Data Fig. 2, showing a polarization oscillation measurement with a temporal resolution suitable to resolve frequencies of 200 GHz and beyond (black), in relation to the intensity

relaxation oscillations on a longer timescale (grey), where the latter measurement involves a longer time window but a reduced temporal resolution.

Modulation efficiency. We investigate the frequency dependence of the amplitude of polarization oscillations. We expect that the amplitude depends on the difference between the lasing mode gain and the non-lasing mode gain, whereas the latter decreases over the range of birefringence splitting used. For this investigation, we calculate from the static spectra an expected amplitude measure for the polarization oscillation amplitude via[87] $A_{\mathrm{PO,s}} = 2\sqrt{I_{\mathrm{NL}}/I_{\mathrm{L}}}$, where I_{NL} and I_{L} are the non-lasing and lasing mode intensities, respectively.

We determine a measure for the oscillation amplitude $A_{\mathrm{PO,d}}$ from the measured dynamics in the temporal signal. For the purpose of comparison, normalized $A_{\mathrm{PO,s}}$ and $A_{\mathrm{PO,d}}$ are depicted in Extended Data Fig. 3. The solid lines show exponential fits. In our experiment, increasing the birefringence-induced mode splitting results in a lower oscillation amplitude. However, this behaviour is not unalterable, but a consequence of the spectral gain shape and the detuning between the gain peak and the cavity mode. The VCSELs used in the experiment were not optimized for polarization modulation at high frequencies. By choosing a suitable detuning, the VCSEL could be designed to obtain a reduced gain difference or dichroism between lasing and non-lasing mode for high birefringence-induced mode splittings. This would lead to larger amplitudes for the polarization oscillations at high frequencies and would additionally affect the damping of the oscillations.

Generalized spin-flip model. To simulate the dynamics of the spin-laser we generalize the spin-flip model[67]. The generalized rate equations expressed with normalized quantities are

$$\dot{E}^{\pm} = [1\,/\,(2\tau_{\mathrm{p}})](1+i\alpha)(N\pm n-1)E^{\pm} - (\gamma_{\mathrm{a}}+i\gamma_{\mathrm{p}})E^{\mp} - (\epsilon_{\mathrm{a}}+i\epsilon_{\mathrm{p}})\,|E^{\pm}|^{2}\,E^{\pm} \quad (5)$$

$$\dot{N} = \gamma\,[J_{-}(t)+J_{+}(t)] - \gamma N - \gamma(N+n)\,|E^{+}|^{2} - \gamma(N-n)\,|E^{-}|^{2} \quad (6)$$

$$\dot{n} = \gamma\,[J_{-}(t)-J_{+}(t)] - \gamma_{\mathrm{s}} n - \gamma(N+n)\,|E^{+}|^{2} + \gamma(N-n)\,|E^{-}|^{2} \quad (7)$$

where $E^{\pm}$ are the right (+) and left (−) circularly polarized components of slowly varying amplitudes of the electric field, and the photon densities are $S^{\pm} = |E^{\pm}|^2$. Since measured intensities are proportional to the corresponding (normalized) photon densities, the normalized intensities are equal to $S^{\pm}$. The photon lifetime is τ_{p}, N is the total population inversion of laser upper and lower levels with a decay rate γ, n is the population difference between spin-down and spin-up electrons with a decay rate γ_{s} due to spin relaxation, $J_{\pm}(t)$ are the time-dependent pumping/injection rates of spin-up (+) and spin-down (−) carriers (for simplicity referred to as current in the following), γ_{a} and γ_{p} are, respectively, the amplitude and phase anisotropies of the cavity (also known as dichroism and birefringence), and α is the linewidth enhancement factor. The relation between the polarization of light and the spin polarization of recombining carriers is given by the standard dipole selection rules in semiconductors[3]. Since holes typically have a negligibly short spin relaxation time, only the electrons are considered spin-polarized[3].

In the standard spin-flip model[67], the polarization of the active region material was assumed to respond linearly to the electric field. Since the standard model failed to describe all experimental observations, we have generalized it in order to account for additional saturation effects. For this purpose a nonlinear response has been included, such that the polarization is $P_{\pm} = (\chi_{\pm} - \tilde{\epsilon}\,|E^{\pm}|^{2})E^{\pm}$. Here, an intensity-dependent part with a complex coefficient $\tilde{\epsilon} = \epsilon_{\mathrm{a}} + i\epsilon_{\mathrm{p}}$ is subtracted from the linear susceptibility $\chi_{\pm}$ to quantify saturation effects associated with amplitude and phase of the field, respectively. This leads to the additional term $-(\epsilon_{\mathrm{a}} + i\epsilon_{\mathrm{p}})|E^{\pm}|^2E^{\pm}$ in equation (5) in comparison to the model used in ref. [67]. Our generalization of the spin-flip model was employed for the calculation of impulse responses and modulation bandwidths, as well as eye diagrams for spin-lasers which were first considered in ref. [65].

Simulation details. In this section we introduce further details of the simulation, parameter sets and their determination.

The excitation pulses that model the experimental behaviour demonstrated in Fig. 2 of the main text were implemented in the simulation as Gaussian pulses. The overall pulse amplitude η_{pulse} is included in the normalized pumping terms for right and left circularly polarized electric fields $J_{+}(t)$ and $J_{-}(t)$ according to

$$J_{\pm}(t) = \eta_{\mathrm{pulse}}\frac{1\pm P_{\mathrm{opt}}}{\tau_{\mathrm{pulse}}\sqrt{2\pi}}\exp\left(-\frac{2t^{2}}{\tau_{\mathrm{pulse}}^{2}}\right) + \frac{J_0}{2} \quad (8)$$

where P_{opt} is the circular polarization degree of the optical pumping and τ_{pulse} is the pulse width parameter. The total pump is $J = J_{+} + J_{-}$. The resulting pump polarization[68] is $P_J = (J_{+} - J_{-})/(J_{+} + J_{-})$.

In the main text, simulations of the modulation bandwidth are shown in Fig. 3a, b and 4a, b. We introduced the modulation of the pumping circular polarization degree according to

$$P_J(t) = P_0 + \delta P\sin(2\pi ft) \quad (9)$$

where δP is the amplitude of polarization modulation. In this section we further introduced the pumping of the intensity modulation

$$J(t) = J_0 + \delta J\sin(2\pi ft) \quad (10)$$

where δJ is the intensity modulation amplitude. The intensity is modulated around the electrical bias pumping J_0. In both cases, the modulation frequency is f.

The corresponding response functions are $R(f) = \delta P_{\mathrm{C}}/\delta P$ for polarization modulation and $R(f) = \delta S/\delta J$ for intensity modulation. δP_{C} and δS are the amplitudes of the modulation responses for polarization and intensity modulation, respectively. Responses are all normalized to their low frequency values at $f_{\mathrm{low}} = 50$ MHz as $\bar{R}(f) = 10\log_{10}[R^2(f)/R^2(f_{\mathrm{low}})]$ and $f_{3\mathrm{dB}}$ is reached when $\bar{R}(f)$ decreases to −3 dB.

The eye diagrams simulated for polarization modulation and intensity modulation (Fig. 3c, d in the main text) result from a pumping approach slightly different to equations (9) and (10). Here, the sinusoidal modulation is replaced by a binary pseudorandom bit stream with a conventional non-return-to-zero coding. The bit stream was filtered in advance with a raised-cosine filter in order to reduce parasitic ringing effects[65].

We use the generalized spin-flip model to reproduce the experimental behaviour theoretically. In order to obtain a good agreement for all experiments simultaneously, the parameter set was carefully determined.

The normalized electrical bias pumping term J_0/J_{th} was measured via the light versus current characteristics as a function of the birefringence. The linear birefringence γ_{p} was obtained from the spectral mode splitting. The circular polarization degree of the optical pumping P was determined according to the combination of the main axes of the linear polarizer and the quarter-wave plate in the pumping beam. The effective dichroism γ_0 is determined by measurement as described in the next section. The pulse width parameter τ_{pulse} is determined from the experimental pulse width of approximately 2 ps.

In addition to the presented polarization and intensity dynamics, a series of measurements for varying pumping conditions and varying birefringence was performed. By obtaining an appropriate fit of the simulation using the generalized spin-flip model to the entirety of our experimental results, we could determine the following from the intensity dynamics: pulse amplitude, carrier decay rate γ, photon lifetime τ_{p}, and phase and amplitude saturation factors $\epsilon_{\mathrm{p,a}}$. Similarly, from the corresponding polarization dynamics we obtained the linewidth enhancement factor α and the spin decay rate γ_{s}.

All the parameter names we use here and their symbols are given in Extended Data Table 1, and the parameter sets for all the simulations presented in this work are given in Extended Data Tables 2–5.

Dichroism. The dichroism generally depends on the cavity mode position as well as the asymmetry of the gain spectrum and is a function of the birefringence-induced mode splitting. The effective dichroism γ_0 is measured[69] by relating the half spectral widths of the two orthogonal lasing and non-lasing modes at half their maxima (HWHM) according to:

$$\gamma_0 = 2\pi(\mathrm{HWHM}_{\mathrm{nonlasing}} - \mathrm{HWHM}_{\mathrm{lasing}}) \quad (11)$$

Using a scanning Fabry–Pérot interferometer with a free spectral range (FSR) of 10 GHz, we determined the dichroism for mode splitting values up to approximately $\Delta f = 45$ GHz, where the increasing mode width exceeds the FSR. We find a linear relation between effective dichroism and birefringence induced-mode splitting. For higher splittings a linear extrapolation is used as the simplest approach. The linear dichroism γ_{a} is calculated in the perturbative regime by

$$\gamma_{\mathrm{a}} = -\frac{1}{2}(\gamma_0 - \gamma_{\mathrm{a}}^{\mathrm{non}}) \quad (12)$$

where the nonlinear dichroism in the perturbative regime is

$$\gamma_{\mathrm{a}}^{\mathrm{non}} = \frac{\gamma S_0}{2\tau_{\mathrm{p}}(\gamma_{\mathrm{s}}^{2} + 4\gamma_{\mathrm{p}}^{2})}(\gamma_{\mathrm{s}} + 2\alpha\gamma_{\mathrm{p}}) + \frac{\epsilon_{\mathrm{a}}}{2}S_0 \quad (13)$$

following the generalized spin-flip model. On the basis of the measured effective birefringence, measured and extrapolated effective dichroism and the pumping condition known from the d.c. pumping, we calculated $\gamma_{\mathrm{a}} = 4.76\ \mathrm{ns}^{-1}$ ($\gamma_{\mathrm{a}} = -1.63\ \mathrm{ns}^{-1}$) for $\Delta f = 42$ GHz ($\Delta f = 214$ GHz). A minor threshold reduction with increasing birefringence was also considered.

We numerically investigated the possibly limiting influence of the dichroism on the polarization modulation dynamics for linear dichroisms between 2 ns^{-1} and

20 ns^{-1} (Extended Data Fig. 4). Increasing absolute values $|\gamma_a|$ (negative parameters were investigated but not shown here for simplicity) lead to a significant damping of the polarization oscillations and thus of the modulation resonance, whereas the 3 dB bandwidth is not affected for values up to 20 ns^{-1}. Consequently the linear dichroism is not considered to be a limiting factor for ultrafast polarization modulation in the investigated range of operation. However, if the effective dichroism is approaching a minimum, the situation can be different. In this regime of bistability, close to a polarization switching point of the VCSEL, the damping of the polarization oscillations is very weak[38] and strong continuous oscillations at the resonance frequency can be observed, as investigated by Torre et al. recently[15]. However, this regime is typically not advantageous for optical communication owing to its strong and narrow resonance in the modulation response, leading to degraded eye diagrams due to strong ringing effects.

Experiments on polarization modulation bandwidth. The polarization dynamics of spin-VCSELs under continuously modulated spin-pumping are investigated in order to experimentally confirm the broad polarization modulation response as described by the generalized spin-flip model and verify that its resonance frequency and bandwidth can be enhanced by increasing the birefringence-induced mode splitting Δf. For this investigation the Ti:sapphire laser for pulsed spin-pumping is replaced by a 760 nm semiconductor laser diode in continuous wave operation. The laser emission is transmitted through a Michelson interferometer of which one arm contains an optical phase modulator electrically driven with a sinusoidal signal. The maximum modulation frequency is limited by the phase modulator to around 25 GHz. With this set-up the circular polarization degree can be modulated, whereas the intensity stays constant. The average power of the pump light is 11 mW. The VCSEL is electrically pumped at $5.4J_{th}$. Δf is measured with an optical spectrum analyser. For diagnostics, the beam path towards the streak camera is equipped with polarization optics, enabling sampling of one of the circular modes. The measurement data include the temporal dynamics of the circularly polarized intensities of both the VCSEL output and the pump light reflection at the VCSEL surface. Thus it is possible to simultaneously investigate the pump amplitude and the VCSEL response amplitude. The pump and response circular intensity traces show an oscillation. For each frequency the pump amplitude A_p and the response amplitude A_r are determined. The response amplitude is corrected by the respective pumping amplitude via $A_{r,c} = A_r/A_p$. The first low-frequency values at 2 GHz and slightly above are averaged and used to normalize $A_{r,c}$ to that value. We have verified that in our case the modulation response curves obtained from a single circular mode are identical to the curves obtained directly from the circular polarization degree.

We obtain modulation responses as depicted in Extended Data Fig. 5a. The experimental data contain response resonance peaks at frequencies corresponding to the birefringence-induced mode splitting. This proves that the resonance frequency of the polarization modulation response can be tuned by the birefringence-induced mode splitting as well as the polarization oscillations. The simulations in Extended Data Fig. 5b using our parameter set obtained in this work resemble the resonance peaks from the experiment. The maximum investigated frequency is only limited by the phase modulator. To the best of our knowledge, no faster phase modulator is available at the used wavelength.

Experimental results for the polarization modulation response in 1.55-μm VCSELs have been presented recently by N. Yokota et al.[25]. They demonstrated a resonance in the polarization modulation response due to a birefringence-induced splitting of 19 GHz, which represents further verification of the concept of polarization modulation. Furthermore, it shows that the concept can be directly adapted to InAlGaAs-VCSELs in the 1.55 μm wavelength range.

Data availability

The data sets generated and analysed in this work are available from the corresponding author on reasonable request.

34. Gordón, C., Guzmán, R., Corral, V., Lo, M. C. & Carpintero, G. On-chip multiple colliding pulse mode-locked semiconductor laser. *J. Lightwave Technol.* **34**, 4722–4728 (2016).
35. Koenig, S. et al. Wireless sub-THz communication system with high data rate. *Nat. Photon.* **7**, 977–981 (2013).
36. Paiella, R. et al. High-frequency modulation without the relaxation oscillation resonance in quantum cascade lasers. *Appl. Phys. Lett.* **79**, 2526–2528 (2001).
37. Li, M. et al. Birefringence controlled room-temperature picosecond spin dynamics close to the threshold of vertical-cavity surface-emitting laser devices. *Appl. Phys. Lett.* **97**, 191114 (2010).
38. Gerhardt, N. C. et al. Ultrafast spin-induced polarization oscillations with tunable lifetime in vertical-cavity surface-emitting lasers. *Appl. Phys. Lett.* **99**, 151107 (2011).
39. Al-Seyab, R., Alexandropoulos, D., Henning, I. & Adams, M. Instabilities in spin-polarized vertical-cavity surface-emitting lasers. *IEEE Photon. J.* **3**, 799–809 (2011).
40. Höpfner, H., Lindemann, M., Gerhardt, N. C. & Hofmann, M. R. Controlled switching of ultrafast circular polarization oscillations in spin-polarized vertical-cavity surface-emitting lasers. *Appl. Phys. Lett.* **104**, 022409 (2014).
41. Nishizawa, N., Nishibayashi, K. & Munekata, H. A spin light emitting diode incorporating ability of electrical helicity switching. *Appl. Phys. Lett.* **104**, 111102 (2014).
42. Hsu, F.-K., Xie, W., Lee, Y.-S., Lin, S.-D. & Lai, C.-W. Ultrafast spin-polarized lasing in a highly photoexcited semiconductor microcavity at room temperature. *Phys. Rev. B* **91**, 195312 (2015).
43. Rudolph, J., Hägele, D., Gibbs, H., Khitrova, G. & Oestreich, M. Laser threshold reduction in a spintronic device. *Appl. Phys. Lett.* **82**, 4516–4518 (2003).
44. Rudolph, J., Döhrmann, S., Hägele, D., Oestreich, M. & Stolz, W. Room-temperature threshold reduction in vertical-cavity surface-emitting lasers by injection of spin-polarized electrons. *Appl. Phys. Lett.* **87**, 241117 (2005).
45. Gøthgen, C., Oszwałdowski, R., Petrou, A. & Žutić, I. Analytical model of spin-polarized semiconductor lasers. *Appl. Phys. Lett.* **93**, 042513 (2008).
46. Vurgaftman, I., Holub, M., Jonker, B. & Meyer, J. Estimating threshold reduction for spin-injected semiconductor lasers. *Appl. Phys. Lett.* **93**, 031102 (2008).
47. Basu, D., Saha, D. & Bhattacharya, P. Optical polarization modulation and gain anisotropy in an electrically injected spin laser. *Phys. Rev. Lett.* **102**, 093904 (2009).
48. Holub, M. & Jonker, B. Threshold current reduction in spin-polarized lasers: role of strain and valence-band mixing. *Phys. Rev. B* **83**, 125309 (2011).
49. Schires, K. et al. Optically-pumped dilute nitride spin-VCSEL. *Opt. Express* **20**, 3550–3555 (2012).
50. Lee, J., Bearden, S., Wasner, E. & Žutić, I. Spin-lasers: from threshold reduction to large-signal analysis. *Appl. Phys. Lett.* **105**, 042411 (2014).
51. Faria, P. E. Jr, Xu, G., Chen, Y.-F., Sipahi, G. M. & Žutić, I. Wurtzite spin lasers. *Phys. Rev. B* **95**, 115301 (2017).
52. Basu, D. et al. Electrically injected InAs/GaAs quantum dot spin laser operating at 200 K. *Appl. Phys. Lett.* **92**, 091119 (2008).
53. Ando, H., Sogawa, T. & Gotoh, H. Photon-spin controlled lasing oscillation in surface-emitting lasers. *Appl. Phys. Lett.* **73**, 566–568 (1998).
54. Hövel, S. et al. Spin controlled optically pumped vertical cavity surface emitting laser. *Electron. Lett.* **41**, 251–253 (2005).
55. Gerhardt, N. C. et al. Enhancement of spin information with vertical cavity surface emitting lasers. *Electron. Lett.* **42**, 88–89 (2006).
56. Hövel, S. et al. Optical spin manipulation of electrically pumped vertical-cavity surface-emitting lasers. *Appl. Phys. Lett.* **92**, 041118 (2008).
57. Fujino, H., Koh, S., Iba, S., Fujimoto, T. & Kawaguchi, H. Circularly polarized lasing in a (110)-oriented quantum well vertical-cavity surface-emitting laser under optical spin injection. *Appl. Phys. Lett.* **94**, 131108 (2009).
58. Frougier, J. et al. Control of light polarization using optically spin-injected vertical external cavity surface emitting lasers. *Appl. Phys. Lett.* **103**, 252402 (2013).
59. Alharthi, S. S. et al. Control of emitted light polarization in a 1310 nm dilute nitride spin-vertical cavity surface emitting laser subject to circularly polarized optical injection. *Appl. Phys. Lett.* **105**, 181106 (2014).
60. Fördös, T. et al. Eigenmodes of spin vertical-cavity surface-emitting lasers with local linear birefringence and gain dichroism. *Phys. Rev. A* **96**, 043828 (2017).
61. Fördös, T. et al. Mueller matrix ellipsometric study of multilayer spin-VCSEL structures with local optical anisotropy. *Appl. Phys. Lett.* **112**, 221106 (2018).
62. Alharthi, S. S. et al. Circular polarization switching and bistability in an optically injected 1300 nm spin-vertical cavity surface emitting laser. *Appl. Phys. Lett.* **106**, 021117 (2015).
63. Lee, J., Falls, W., Oszwałdowski, R. & Žutić, I. Spin modulation in semiconductor lasers. *Appl. Phys. Lett.* **97**, 041116 (2010).
64. Saha, D., Basu, D. & Bhattacharya, P. High-frequency dynamics of spin-polarized carriers and photons in a laser. *Phys. Rev. B* **82**, 205309 (2010).
65. Wasner, E., Bearden, S., Lee, J. & Žutić, I. Digital operation and eye diagrams in spin-lasers. *Appl. Phys. Lett.* **107**, 082406 (2015).
66. Boéris, G., Lee, J., Výborný, K. & Žutić, I. Tailoring chirp in spin-lasers. *Appl. Phys. Lett.* **100**, 121111 (2012).
67. San Miguel, M., Feng, Q. & Moloney, J. Light-polarization dynamics in surface-emitting semiconductor lasers. *Phys. Rev. A* **52**, 1728–1739 (1995).
68. Gahl, A., Balle, S. & San Miguel, M. Polarization dynamics of optically pumped VCSELs. *IEEE J. Quantum Electron.* **35**, 342–351 (1999).
69. van Exter, M., Willemsen, M. & Woerdman, J. Polarization fluctuations in vertical-cavity semiconductor lasers. *Phys. Rev. A* **58**, 4191–4205 (1998).
70. Ackemann, T. & Sondermann, M. Characteristics of polarization switching from the low to the high frequency mode in vertical-cavity surface-emitting lasers. *Appl. Phys. Lett.* **78**, 3574–3576 (2001).
71. Sondermann, M., Weinkath, M. & Ackemann, T. Polarization switching to the gain disfavored mode in vertical-cavity surface-emitting lasers. *IEEE J. Quantum Electron.* **40**, 97–104 (2004).
72. Willemsen, M. B., van Exter, M. P. & Woerman, J. P. Anatomy of a polarization switch of a vertical-cavity semiconductor laser. *Phys. Rev. Lett.* **84**, 4337–4340 (2000).
73. Blansett, E. L. et al. Ultrafast polarization dynamics and noise in pulsed vertical-cavity surface-emitting lasers. *Opt. Express* **9**, 312–318 (2001).
74. Virte, M., Panajotov, K., Thienpont, H. & Sciamanna, M. Deterministic polarization chaos from a laser diode. *Nat. Photon.* **7**, 60–65 (2013).
75. Panajotov, K. et al. Impact of in-plane anisotropic strain on the polarization behavior of vertical-cavity surface-emitting lasers. *Appl. Phys. Lett.* **77**, 1590–1592 (2000).

76. Ostermann, J., Debernardi, P., Kroner, A. & Michalzik, R. Polarization-controlled surface grating VCSELs under externally induced anisotropic strain. IEEE Photon. *Technol. Lett.* **19**, 1301–1303 (2007).
77. Ostermann, J. M. & Michalzik, R. in *VCSELs* (ed. Michalzik, R.) Ch. 5, 147–179 (Springer, Berlin, 2013).
78. Long, C. M. et al. Polarization mode control of long-wavelength VCSELs by intracavity patterning. *Opt. Express* **24**, 9715–9722 (2016).
79. Kawaguchi, H. Bistable laser diodes and their applications: state of the art. *IEEE J. Sel. Top. Quantum Electron.* **3**, 1254–1270 (1997).
80. Bretenaker, F. & Floch, A. L. The dynamics of spatially-resolved laser eigenstates. *IEEE J. Quantum Electron.* **26**, 1451–1454 (1990).
81. Alouini, M. et al. Offset phase locking of Er,Yb:glass laser eigenstates for RF photonics applications. IEEE Photon. *Technol. Lett.* **13**, 367–369 (2001).
82. Carpintero, G. et al. Wireless data transmission at terahertz carrier waves generated from a hybrid InP-polymer dual tunable DBR laser photonic integrated circuit. *Sci. Rep.* **8**, 3018 (2018).
83. Badr, N., White, I. H., Tan, M. R. T., Houng, Y. M. & Wang, S. Y. Enhanced polarisation self-switching in a vertical-cavity surface-emitting laser by gain saturation of transverse modes. *Electron. Lett.* **30**, 1227–1229 (1994).
84. Dems, M., Czyszanowski, T., Thienpont, H. & Panajotov, K. Highly birefringent and dichroic photonic crystal VCSEL design. *Opt. Commun.* **281**, 3149–3152 (2008).
85. Pusch, T. et al. Birefringence tuning of VCSELs. *Proc. SPIE* **9892**, 989222 (2016).
86. Berry, H. G., Gabrielse, G. & Livingston, A. E. Measurement of the Stokes parameters of light. *Appl. Opt.* **16**, 3200–3205 (1977).
87. Jackson, J. D. *Classical Electrodynamics* (Wiley, New York, 1999).

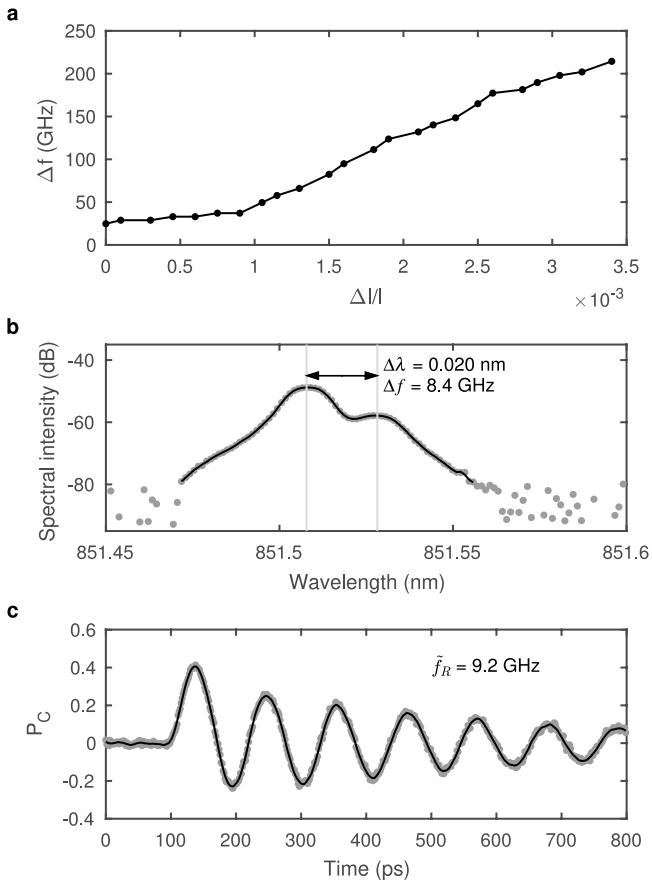

Extended Data Fig. 1 | Strain-dependent behaviour. a, Strain $\Delta l/l$ and the resulting mode splitting Δf. Points show determined values, lines are their direct connections and are included for improved visualization. **b**, Spectrum without applied external strain. The vertical lines mark the maxima of the two orthogonal modes. The arrow indicates the resulting Δf. The solid line is a smoothed curve through the raw data (points). **c**, Corresponding polarization oscillation in the circular polarization degree P_C with a frequency of 9.2 GHz. The solid line is a smoothed curve through the raw data (points).

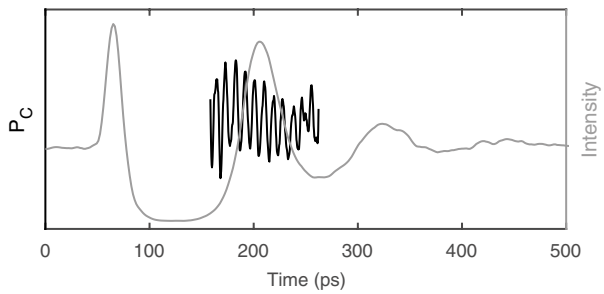

Extended Data Fig. 2 | Acquisition timing. Shown is the trace of the intensity obtained with the streak camera for a long measurement window (grey) and the trace of the circular polarization degree for a short measurement window with higher temporal resolution (black). The positioning of the shorter measurement window for acquisition of fast polarization oscillations over the full scale of the dynamic process caused by the spin injection pulse is evident.

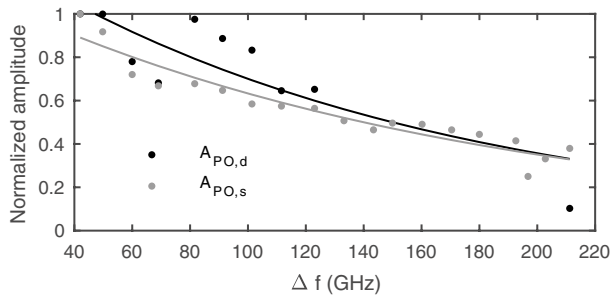

Extended Data Fig. 3 | Modulation efficiency. The figure shows how polarization oscillation amplitudes depend on the birefringence-induced mode splitting. Grey trace, calculated amplitude $A_{PO,d}$ derived from the spectrum by relating the intensities of lasing and non-lasing modes. Black trace, actual polarization oscillation amplitude $A_{PO,s}$ from the temporal traces. Points mark raw data, lines show exponential fits. For splittings between 130 and 200 GHz no data are shown as the amplitude is quite close to the noise level of the streak camera. The data points in Fig. 2c were obtained by Fourier transform from these data. At 214 GHz the streak camera was used in another mode of measurement offering a better signal-to-noise ratio. For constant applied spin-injection, the resulting polarization oscillation amplitude and thus the modulation efficiency decreases with increasing mode splitting.

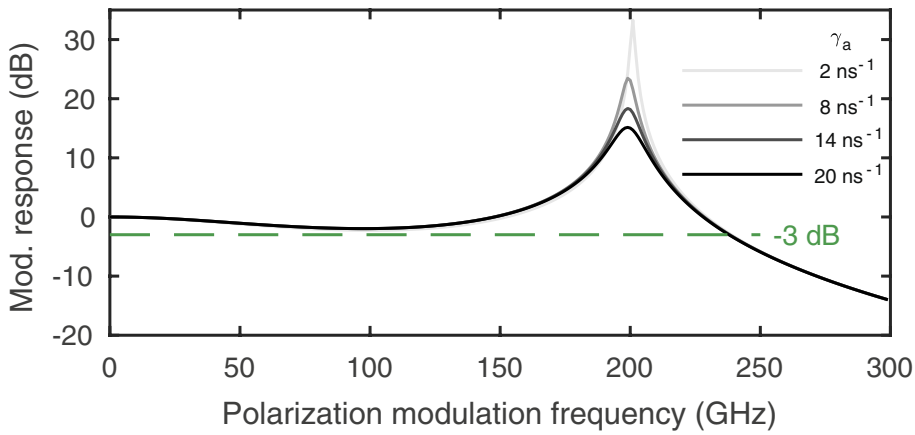

Extended Data Fig. 4 | Dichroism dependent polarization modulation response curves. Plots show simulated modulation (Mod.) response as a function of polarization modulation frequency for different values of dichroism γ_a (see key). The dashed green line marks the −3dB level as a measure for the lower limit of the desired modulation response.

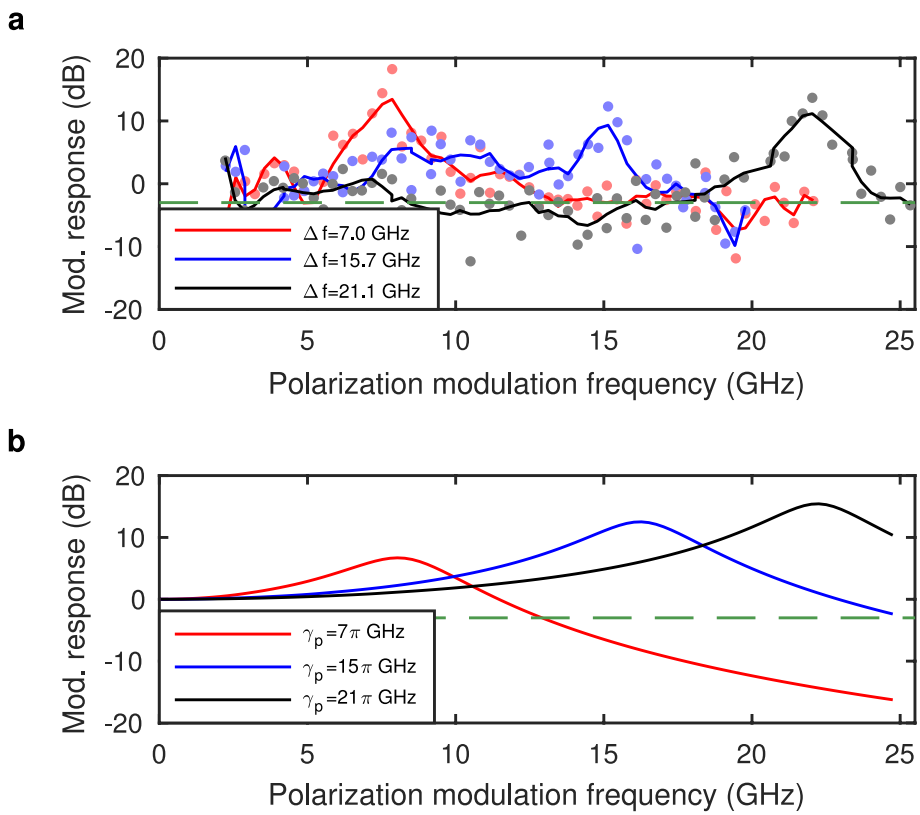

Extended Data Fig. 5 | Experimental polarization modulation and its birefringence dependence. a, Results for several values of the birefringence-induced mode splitting, Δf (see key). Points mark raw data, lines are smoothed data. **b**, Numerical verification of results in **a** using the parameter set obtained in this work for the appropriate values of γ_p (see key).

Extended Data Table 1 | List of symbols used in the simulations

Symbol	Parameter
J_0	Electrical bias current
η_{pulse}	Pulse amplitude
τ_{pulse}	Optical pump pulse width parameter
P_{opt}	Circular polarization degree of optical pumping
δJ	Intensity modulation amplitude
δP	Polarization modulation amplitude
P_0	Polarization modulation offset
f	Modulation frequency
N_{bits}	Number of random bits
R_{bits}	Bit rate
α	Linewidth enhancement factor
γ	Carrier decay rate
τ_p	Photon lifetime
γ_s	Spin decay rate
γ_a	Linear dichroism
γ_p	Linear birefringence
ε_a	Amplitude saturation factor
ε_p	Phase saturation factor

Extended Data Table 2 | Spin-flip model parameters for Fig. 2

Symbol	Fig. 2a	Fig. 2b	Fig. 2c
J_0	$5.2 \cdot J_{th}$	$5.4 \cdot J_{th}$	$4.94 - 5.4 \cdot J_{th}$
η_{pulse}	0.15	0.12	0.15
τ_{pulse}	1.5 ps	1.5 ps	1.5 ps
P_{opt}	1 (right)	1 (right)	1 (right)
α	5	5	5
γ	1 ns^{-1}	1 ns^{-1}	1 ns^{-1}
τ_p	1.54 ps	1.54 ps	1.54 ps
γ_s	450 ns^{-1}	450 ns^{-1}	450 ns^{-1}
γ_a	2.57 ns^{-1}	-1.63 ns^{-1}	4.77 – -1.77 ns^{-1}
γ_p	111π GHz	211.5π GHz	$40\pi - 215\pi$ GHz
ε_a	1.6	1.6	1.6
ε_p	-3.2	-3.2	-3.2

Extended Data Table 3 | Spin-flip model parameters for Figs. 3a, b, 4a, b

Symbol	Fig. 3a	Fig. 3b	Fig. 4a	Fig. 4b
J_0	1.5 – 9.0 $\cdot J_{th}$	5.4 $\cdot J_{th}$	5.4 $\cdot J_{th}$	1.5 – 9 $\cdot J_{th}$
δJ, δP	3.0 $\cdot J_{th}$	0.25	0.25	0.25
P_0	-	0	0	0
f	0 GHz – 25 GHz	0 – 400 GHz	0 GHz – 300 GHz	0 GHz – 300 GHz
α	5	5	5	5
γ	1 ns^{-1}	1 ns^{-1}	1 ns^{-1}	1 ns^{-1}
τ_p	1.54 ps	1.54 ps	1.54 ps	1.54 ps
γ_s	450 ns^{-1}	450 ns^{-1}	100 – 500 ns^{-1}	450 ns^{-1}
γ_a	-5.12 – 2.49 ns^{-1}	5.34 – -3.11 ns^{-1}	-1.00 – -1.21 ns^{-1}	-5.12 – 2.48 ns^{-1}
γ_p	200π GHz	50 – 250π GHz	200π GHz	200π GHz
ε_a	1.6	1.6	1.6	1.6
ε_p	-3.2	-3.2	-3.2	-3.2

Extended Data Table 4 | Spin-flip model parameters for Fig. 3c, d

Symbol	Fig. 3c	Fig. 3d
J_0	$5.4 \cdot J_{th}$	$5.4 \cdot J_{th}$
δJ, δP	$0.1 \cdot J_{th}$	0.25
P_0	-	0
N_{bits}	1024	1024
R_{bits}	10 – 20 Gbit/s	10 – 240 Gbit/s
α	5	5
γ	1 ns^{-1}	1 ns^{-1}
τ_p	1.54 ps	1.54 ps
γ_s	450 ns^{-1}	450 ns^{-1}
γ_a	-1.16 ns^{-1}	-1.16 ns^{-1}
γ_p	200π GHz	200π GHz
ε_a	1.6	1.6
ε_p	-3.2	-3.2

Extended Data Table 5 | Spin-flip model parameters for Extended Data Fig. 4

Symbol	Extended Data Fig. 4
J_0	$5.4 \cdot J_{th}$
δP	0.25
P_0	0
f	0 GHz – 300 GHz
α	5
γ	1 ns^{-1}
τ_p	1.54 ps
γ_s	450 ns^{-1}
γ_a	2 – 20 ns^{-1}
γ_p	200π GHz
ε_a	1.6
ε_p	-3.2